Pinpointing basic sites formed upon incorporation of iron in hierarchical SAPO-11 using catalytic model reactions

SCHOLARONE™
Manuscripts

Pinpointing basic sites formed upon incorporation of iron in hierarchical SAPO-11 using catalytic model reactions[†]

Daniel Ali[a], Zhihui Li[b], Muhammad Mohsin Azim[a], Hilde Lea Lein[c], Karina Mathisen*[a].

Abstract

By utilizing previously established catalytic model reactions, a method for probing the topological location of transition metal sites incorporated in hierarchical silicoaluminophosphates (SAPOs) is presented. For the first time, iron(III)-incorporated hierarchical SAPO-11 (FeCTAB-11) was prepared and thoroughly characterized with conventional iron(III)-incorporated SAPO-11 (FeSAPO-11) as a reference. Initially, inductively coupled plasma - mass spectrometry (ICP-MS) indicated that the FeSAPOs contained similar amounts of metal (~2.0 wt.%), while N_2-physisorption confirmed the bimodal porosity of the hierarchical FeCTAB-11. Furthermore, X-ray absorption spectroscopy (XAS) revealed that iron(III) was isomorphously incorporated into both SAPO-11 samples, whereas CO_2-temperature programmed desorption (TPD) revealed the first reported presence of strong basic sites in the vicinity of a transition metal incorporated into a SAPO framework. The location of the basic sites, and thus the incorporated iron, was subsequently probed by studying the products of the base-catalyzed vapor phase isomerization of cyclohexanone oxime (Beckmann rearrangement, BMR) model reaction. Through an increased lifetime for the base-catalyzed production of aniline, the incorporated iron for FeCTAB-11 was found to be located in highly accessible mesopores, whereas the conventional FeSAPO-11 had incorporated iron located in its micropores. Lastly, the methanol-to-hydrocarbons (MTH) model reaction showed that both FeSAPOs only had Brønsted acid sites in the micropores of the structures. This was used to verify the pore connectivity of the hierarchical FeCTAB-11 by utilizing the base-catalyzed BMR mechanism's dependency on acid sites.

[a]Department of Chemistry, Norwegian University of Science and Technology (NTNU), N-7491 Trondheim Norway. *Corresponding author. E-mail: karina.mathisen@ntnu.no

[b]Department of Chemical Engineering, NTNU, N-7491 Trondheim Norway

[c]Department of Materials Science and Engineering, NTNU, N-7491 Trondheim Norway

[†]Electronic Supplementary Information (ESI) available.

1. Introduction

The incorporation of transition metals (e.g. Cu, Fe or Ni) into various silicoaluminophosphates (SAPOs) has been extensively studied in order to broaden and enhance the inherent catalytic activity of the SAPOs.[1–3] Transition metal-incorporated SAPOs have for instance been shown to be highly active for the selective catalytic reduction (SCR) of nitrogen oxides (NOx) by ammonia[1,4] and the methanol-to-olefins (MTO) reaction.[5,6] Furthermore, whereas SAPOs are intrinsically acidic materials, the incorporation of metal may also create basic sites.[7] This opens up possibilities for SAPOs to be utilized in base-catalyzed reactions and potentially also in carbon dioxide (CO_2) capture processes.[8] However, while several studies report the enhanced performance of transition metal-incorporated conventional SAPOs,[1–6] few have ventured beyond metal-incorporation to also simultaneously address the inherent diffusion limitations that arise due to the microporous framework of SAPOs.[9,10] Indeed, while there are many studies on hierarchical SAPOs,[10–15] research on the incorporation of transition metals into hierarchical SAPOs is scarce.[13–16]

A critical issue in the incorporation of transition metals into hierarchical SAPOs is the topological location of the metal.[16] Indeed, similar to the location of the Brønsted acid sites, the location of the transition metal dictates the contributing effect of the mesopores in the hierarchical structure. For shape selective reactions (e.g. MTO), the metal should ideally be located in the micropores to retain the shape selective effects of these pores.[7] However, for reactions that depend on the accessibility of the metal (e.g. SCR of NOx), transition metal sites in mesopores would lead to a longer lifetime.[16] Previously, we have demonstrated that the methanol-to-hydrocarbons (MTH) model reaction can function as a characterization technique for locating the Brønsted acid sites and probing the pore connectivity of high acid density hierarchical SAPO-5 (12-membered ring, 0.7 nm pore apertures).[17,18] Likewise, the corresponding properties of the low acid density hierarchical SAPO-11 (10-membered ring, 0.4 nm × 0.6 nm pore apertures)[17] were successfully investigated by using the vapor phase isomerization of cyclohexanone oxime (Beckmann rearrangement, BMR) model reaction.[19] With this work, we wish to demonstrate the versatility of the previously introduced model reactions by probing the pore connectivity and location of transition metal sites in a metal-incorporated hierarchical SAPO model system.

In this study, the topological location of an isomorphously substituted transition metal in a hierarchical SAPO model system was probed with model reactions. Iron was chosen as the transition metal and hierarchical SAPO-11 was chosen as the model system with cetyltrimethylammonium bromide (CTAB) applied as a mesopore structure-directing agent. A conventional iron-incorporated SAPO-11 was also synthesized as a reference system. To probe the phase purity, pore characteristics and acid/base properties of the SAPOs, the molecular sieves were initially comprehensively characterized. X-ray absorption spectroscopy was additionally employed to investigate if the iron was successfully incorporated into the SAPO structures. Subsequently, the topological location of the iron species was elucidated by utilizing the base-catalyzed BMR, whereas the MTH model reaction was applied to probe the Brønsted acid site location of the iron-incorporated SAPO-11s. Finally, the pore connectivity of the hierarchical sample was probed by a combined study of the location of the acid sites and the mechanism of the base-catalyzed BMR model reaction.

2. Experimental

2.1 Synthesis of samples

2.1.1 Iron-incorporated conventional and hierarchical SAPO-11

The conventional iron-incorporated SAPO-11 was hydrothermally synthesized by modifying the previously reported procedure for synthesis of conventional SAPO-11.[19] An initial solution of iron(II) acetate (Fe(OAc)$_2$, 0.314 g, 1.7 mmol, Sigma Aldrich, 99%) in deionized water (H$_2$O, 57.39 g, 3188 mmol) was stirred until homogeneous, after which aluminium isopropoxide (Al(O-i-Pr)$_3$, 11.03 g, 53 mmol, Sigma Aldrich, ≥98%) was added and the mixture was again stirred until homogeneous. Following this, phosphoric acid (H$_3$PO$_4$, 6.22 g, 54 mmol, Merck, 85%) was added dropwise and the resulting mixture was stirred for 1 hour. Subsequently, tetraethyl orthosilicate (TEOS, 1.13 g, 5.3 mmol, Sigma Aldrich, 98%) was added and the mixture was stirred for 2 hours before dropwise addition of the micropore structure-directing agents (micro-SDAs), dipropylamine (DPA, 1.64 g, 16 mmol, Fluka, ≥99%) and diisopropylamine (DIPA, 1.64g, 16 mmol, Sigma Aldrich, 99%). After stirring for an additional 2 hours, the final mixture, with a theoretical composition of 1.0Al : 1.0P : 0.1Si : 0.3DPA : 0.3DIPA: 61H$_2$O : 0.033Fe, was adjusted to pH 6.0 using phosphoric acid before

being poured into a 60 mL Teflon-lined stainless-steel autoclave for crystallization at 170 °C for 48 hours. After quenching, the resulting powder was washed three times with deionized water and once with ethanol. The final product, FeSAPO-11, was obtained after drying for 3 hours at 110 °C and finally calcining for 6 hours at 600 °C in air.

Based on the synthesis procedure for the conventional FeSAPO-11, a parameter study was conducted to obtain a synthesis route for the hierarchical iron-incorporated SAPO-11 using cetyltrimethylammonium bromide (CTAB, Sigma Aldrich, >99%) as a mesopore structure-directing agent (meso-SDA). The final synthesis procedure was identical to that of the conventional FeSAPO-11, except for the addition of 0.025 equivalents of CTAB after dissolution of (Al(O-i-Pr)$_3$. The final mixture had a theoretical composition of 1.0Al : 1.0P : 0.1Si : 0.3DPA : 0.3DIPA : 61H$_2$O : 0.033Fe : 0.025CTAB. The crystallization time for the hierarchical iron-incorporated SAPO-11 was 84 hours, while the crystallization temperature, washing, drying and calcination procedures were the same as for the conventional FeSAPO-11. The hierarchical iron-incorporated SAPO-11 was labelled as FeCTAB-11.

2.2 **General characterization**

Specifically for the samples in this study, the phase purity was verified by using X-ray diffraction (XRD) with a Bruker D8 A25 DaVinci X-ray Diffractometer with a CuKα radiation source (1.5406 Å) and LynxEye™ SuperSpeed Detector. Relative crystallinities were calculated according to previously reported methods.[19,20] Detailed experimental information regarding additional characterization techniques (scanning electron microscopy (SEM), inductively coupled plasma - mass spectrometry (ICP-MS), N$_2$-physisorption and Fourier-transform infrared spectroscopy (FTIR)) and post-catalysis investigations by thermogravimetric analysis coupled with mass spectrometry (TGA-MS) has been provided in the electronic supplementary information (ESI, Section 1.1).

Temperature-programmed desorption (TPD) of carbon dioxide (CO$_2$) was carried out to probe the presence of basic sites for the FeSAPOs. Filtered particle size (15 mg, 212 - 425 μm) was inserted into a Netzsch Jupiter STA 449 equipped with a QMS 403 Aëlos quadrupole mass spectrometer. For pre-treatment, samples were heated (ramp rate of 10 °C min^{-1}) and held at 500 °C for 1 hour in a constant flow of argon (55 mL min^{-1}). After cooling to the adsorption

temperature (120 °C), a mixture of CO_2 (30 mL min^{-1}, 99%) and argon (25 mL min^{-1}) was allowed to interact with the sample for 1 hour before flushing for 2 hours with argon (55 mL min^{-1}). Finally, desorption was carried out by heating the sample to 840 °C while flushing with argon and monitoring the signal from CO_2 (m/z 44) with the mass spectrometer (MS).

2.3 **X-ray absorption spectroscopy**

2.3.1 Data collection

X-ray absorption spectroscopy (XAS) data was collected in hybrid filling mode at the Swiss-Norwegian Beamlines (SNBL, BM31) at the European Synchrotron Radiation Facility (ESRF) for the Fe K-edge (7112 eV). A bending magnet produced the white beam for the beamline, where a water-cooled Si[111] double-crystal monochromator was utilized for iron XAS data collection in transmission mode from 6970 to 7900 eV with a respective step size and counting time of 0.5 and 200 ms. The initial (I_0) and transmitted ($I_{1, 2}$) intensities were detected using ion chambers (30 cm), where I_0 had an absorption of 20% and $I_{1, 2}$ had an absorption of 80%.

XAS data was also measured at the Balder beam line at MAX IV. The white beam was collected from the storage ring with an in-vacuum wiggler, where a Si[111] double crystal monochromator was utilized for XAS collection. The initial (I_0) and transmitted ($I_{1,2}$) intensities were detected using ion chambers, where the former was filled with He (0.6 bar) and N_2 (0.9 bar) and the latter with Ar (0.2 bar) and N_2 (1.8 bar). Measurements were conducted using the fly scan mode from 7060 to 7360 eV with a respective step size and counting time of 0.5 eV and 300 ms.

Samples and references were put in aluminum holders and measured ex situ, where the references were also diluted with boron nitride (BN) to avoid saturation.

2.3.2 Data reduction

Athena from the Demeter package[21] was used for data reduction, where the collected data was binned (Edge region -30 to 50 eV; Pre-edge grid 10 eV; X-ray absorption near edge structure (XANES) grid 0.5 eV; extended X-ray absorption fine structure (EXAFS) grid 0.05 Å^{-1}),

energy corrected for iron foil (E_0 = 7112 eV) and normalized. XANES and EXAFS spectra were respectively normalized from 50 - 150 eV and from 150 eV until the end of the scan, where EXAFS spectra were also deglitched and truncated if necessary. The k-edge absorption edge energy (E_0) was selected and set at 0.5 of the normalized absorption spectra.

EXAFS least-square refinements were carried out with DL-EXCURV[22] where the theoretical $\chi_i^{th}(k)$ is fitted to the experimental $\chi_i^{exp}(k)$ using curved wave theory and calculated ab initio phase shifts. The curves were fitted using k^3 weighting with a k-range of 2 - 12 Å^{-1} unless otherwise stated, where the goodness of the fit was evaluated using the statistical R-factor.

2.4 **Model reactions**

In accordance to previous reports,[18] the methanol to hydrocarbons (MTH) model reaction was carried out in a tube reactor (ID: 4 mm). The reaction products were analyzed with a gas chromatograph equipped with a flame ionizing detector (FID) coupled to a mass spectrometer (GC-MS, Agilent 7890A coupled to an Agilent 5975C inert XL MSD).

In a typical experiment, 30 mg of filtered particle size (212 - 425 μm) of calcined FeSAPO-11 was loaded into the reactor before water and other adsorbed impurities were removed by heating the reactor to 500 °C for 1 hour. The reaction was performed at 400 °C by sending chilled methanol (0 °C, VWR, ≥99.8%) carried by helium into the reactor at a Weight Hourly Space Velocity (WHSV) of 1.8 g_{MeOH} g_{cat}^{-1} h^{-1}.

The vapor phase Beckmann rearrangement of cyclohexanone oxime was carried out in a vertical tube reactor (ID: 4 mm) attached to a condenser as described by previous reports.[19] By applying chlorobenzene (99%, Sigma Aldrich) as an internal standard, the obtained liquid products were identified and analyzed with a gas chromatograph equipped with a flame ionizing detector (FID) coupled to a mass spectrometer (GC-MS, Agilent 7890A coupled to an Agilent 5975C inert XL MSD).

In a typical experiment, 30 mg of filtered particle size (212 - 425 μm) of calcined FeSAPO-11 was loaded into the reactor before heating the reactor to 500 °C for 8 hours in He to remove water and other adsorbed impurities. The reaction was performed at 325 °C with a helium flow

of 14 mL min^{-1}. The liquid-feed consisted of 5 g L^{-1} of cyclohexanone oxime (CHO, 99%, Sigma Aldrich) in ethanol and was fed via an electric syringe pump (KD Scientific Legato 210) at a WHSV of 0.79 g_{CHO} g_{cat}^{-1} h^{-1}. The calibration, conversion, selectivity and mass balance calculations were carried out in accordance to previous reports.[18,19]

3. Results & discussion

3.1 General characterization

Initially, a comprehensive characterization was conducted to determine the properties of the iron-containing conventional and hierarchical SAPO-11s. XRD was conducted to probe the phase purities, followed by SEM and ICP-MS analyses which were employed in order to respectively investigate the morphological and elemental properties of the structures. Nitrogen physisorption was subsequently performed to elucidate the texture properties of the materials as well as to investigate the presence of bimodal porosity for the hierarchical FeCTAB-11. Finally, XAS was conducted to investigate the incorporation of iron into the SAPO-11 structures.

The X-ray diffractograms of the calcined conventional FeSAPO-11 and hierarchical FeCTAB-11 are stacked together with the simulated AEL pattern in Fig. 1.[17]
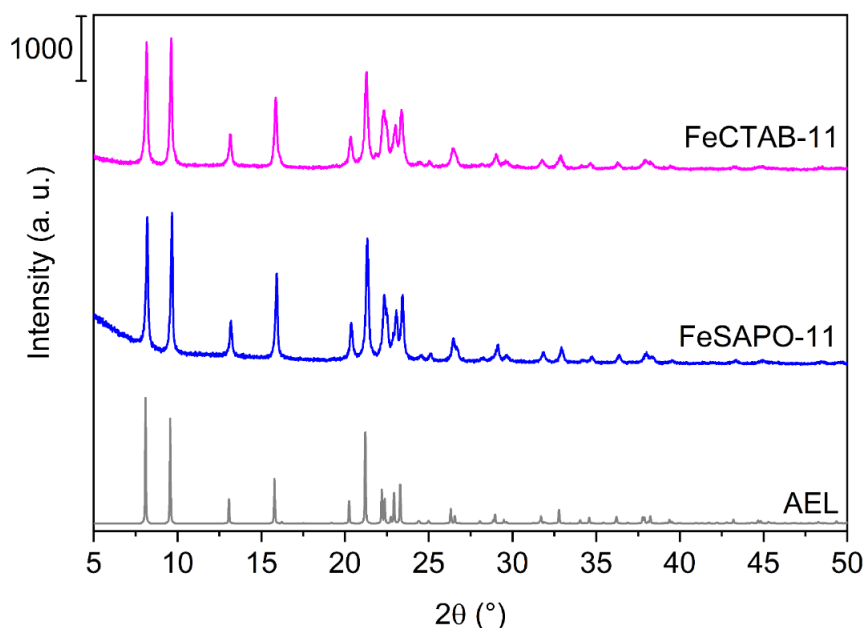

Fig. 1: XRD of calcined FeSAPO-11 and FeCTAB-11 with the AEL structure as a reference.

The diffractograms of the FeSAPOs displayed a crystalline AEL phase and all calcined and as-prepared (Fig. S1-1) samples were phase pure. Indeed, as there were no visible iron oxide phases in the diffractograms, this is a promising preliminary indication on the successful incorporation of iron into the SAPO-11 structure. On the other hand, it should be mentioned that iron may still exist as nanoparticulate iron oxide below the detection limit of XRD (i.e. < 2.0 nm).[23,24] The relative crystallinities of FeSAPO-11 (100%) and FeCTAB-11 (96%) were essentially identical as given in Table 1. While there are few reports on metal-incorporated hierarchical SAPO-11, this result is similar to a report on gold-incorporated conventional and hierarchical SAPO-34, where the relative crystallinity of the hierarchical analogue was identical to that of the conventional AuSAPO-34.[13] It should be noted that the relative crystallinity for FeCTAB-11 is higher than previous reports on hierarchical SAPO-11 (without metal) synthesized with CTAB as a meso-SDA, where the crystallinity was significantly lower (~70%) compared to the conventional SAPO-11.[25]

Table 1: Summary of ICP-MS and nitrogen physisorption characterization results for the FeSAPO-11s.

Sample	RC^a (%)	Fe^b (wt.%)	$Si/Al_T{}^c$	$Si/Al_{ICP}{}^d$	Surface area ($m^2\,g^{-1}$)			Pore volume ($cm^3\,g^{-1}$)	
			Equivalents		S_{BET}	S_{micro}	S_{ext}	V_{micro}	V_{meso}
FeSAPO-11	100	1.9	0.1	0.1	198	135	63	0.07	0.06
FeCTAB-11	96	2.0	0.1	0.1	247	123	124	0.06	0.13

[a]Relative crystallinity.

[b]Amount of iron in calcined samples as obtained by ICP-MS element analysis.

[c]Theoretically calculated gel composition.

[d]Sample composition obtained by ICP-MS element analysis for calcined samples.

The SEM images of the calcined FeSAPO-11s are shown in Fig. 2 whereas images of the as-prepared samples are shown in the ESI, Fig. S1-2. The average particle sizes matched previous reports on non-metal containing conventional and hierarchical SAPO-11[10,26] and were 21 ± 10 and 9 ± 3 μm for FeSAPO-11 and FeCTAB-11, respectively. In agreement with the aforementioned reports, both samples also displayed agglomerates of plates, where the conventional FeSAPO-11 had agglomerates of larger plates compared to FeCTAB-11 (Fig. S1-

3). It should be mentioned that CTAB as a surfactant is known to stabilize smaller particles,[25] and that this may be the reason why FeCTAB-11 has a smaller particle size compared to FeSAPO-11. Lastly, the incorporation of metal into SAPO-34 has been demonstrated to increase or decrease the particle size of the SAPO depending on the metal,[6] indicating that the addition of iron may also have affected the particle size of the FeSAPO-11s in this study.
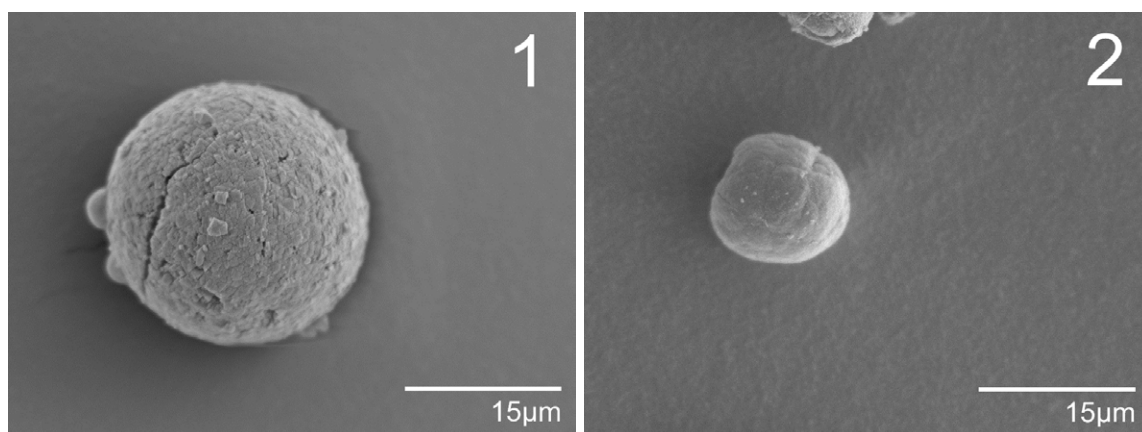

Fig. 2: SEM micrographs of FeSAPO-11 (1) and FeCTAB-11 (2), showing a typical particle for each sample.

ICP-MS results are given in Table 1 and Table S1-1, where the latter also includes an additional comparison to a conventional SAPO-11 reference without metal. The elemental analysis revealed that the FeSAPOs had identical Si/Al ratios (0.1) that matched the theoretically calculated gel compositions, and that the iron-containing molecular sieves also contained comparable amounts of iron (~2.0 wt.%). This indicates that the addition of a meso-SDA to the synthesis of hierarchical FeCTAB-11 did not significantly affect the uptake of iron into the SAPO-11 structure, which is in accordance to a previous report on gold-incorporated hierarchical SAPO-34 synthesized with a surfactant meso-SDA.[13]

The results from nitrogen physisorption analyses (Table 1) showed that the FeSAPO-11s had total apparent surface areas ranging from ~200 - 250 $m^2 g^{-1}$, well within the previously reported range of the SAPO-11 system.[11,12,27,28] Specifically, the micropore surface areas for FeSAPO-11 and FeCTAB-11 were essentially identical (135 and 123 $m^2 g^{-1}$, respectively) while the hierarchical sample had an external surface area that was twice as large (124 $m^2 g^{-1}$) as that of the conventional FeSAPO (63 $m^2 g^{-1}$). These surface areas also correspond to previous studies on non-metal-containing conventional SAPO-11 and hierarchical SAPO-11 synthesized with

CTAB as a meso-SDA, where a comparison to a reference conventional SAPO-11 without metal (C-SAPO-11) has been provided in the ESI, Table S1-2.[10,19,28]

The micropore volumes of the SAPOs in this study were comparable (~0.07 cm^3 g^{-1}), whereas FeCTAB-11 had a much larger mesopore volume (0.13 cm^3 g^{-1}) than FeSAPO-11 (0.06 cm^3 g^{-1}). The micropore volumes were in accordance with previous literature reports,[28,29] whereas the mesopore volumes for both the conventional FeSAPO-11 and the hierarchical FeCTAB-11 were in the lower range of previous studies on non-metal-containing SAPO-11 systems.[12,29] Notably however, both the micropore and mesopore volumes matched a previous study on the hydrothermal synthesis of conventional SAPO-11 and hierarchical SAPO-11 with CTAB as a meso-SDA, where a comparison to the former has been included in the ESI, Table S1-2.[19]

The nitrogen physisorption isotherms of the FeSAPOs are displayed in Fig. 3A, whereas a comparison to a reference C-SAPO-11 has been provided in the ESI, Fig. S1-4A. Altogether, the isotherms resembled previously reported results on the SAPO-11 system.[11,25,29] The conventional FeSAPO-11 displayed a type I(a) isotherm with a small H4 hysteresis loop, which according to the International Union of Pure and Applied Chemistry (IUPAC) is characteristic of materials with narrow micropores or aggregated SAPO crystals.[30] On the other hand, FeCTAB-11 exhibited a type IV(a) isotherm with a saturation plateau at p·p$_0^{-1}$ 0.6 which is typically indicative of the presence of mesopores. Indeed, similar plateaus have previously been shown to occur for mesoporous materials such as SBA-15 and MCM-41[31] as well as for hierarchical SAPO-11 with a high degree of connectivity between micro- and mesopores.[11] Regarding the Barrett-Joyner-Halenda (BJH) pore size distributions (Fig. 3B and Fig. S1-4B), the conventional FeSAPO-11 had a minor feature at 3.3 nm. Similar features have previously been reported to occur for conventional SAPO-11,[11,27,28] where one study attributed the feature to intercrystalline voids between particles of varying size.[27] Indeed, the SEM results for FeSAPO-11 indicated that the sample had a wide particle size distribution (21 ± 10 μm), and the observed BJH feature was therefore ascribed to intercrystalline spacings between particles with varying sizes. Lastly, the hierarchical FeCTAB-11 had a single, distinct feature at 3.5 nm, indicating the presence of a uniform size distribution of mesopores. In other words, the BJH pore size distribution indicated that FeCTAB-11 had a hierarchical pore structure with both micropores and mesopores present in its structure, whereas FeSAPO-11 only had micropores in its structure. As a final note, physisorption studies using nitrogen coupled with BET and BJH analysis is associated with limitations when used to analyze microporous materials.[30]

Therefore, the technique was mainly included in this study to provide a relative comparison between the textural properties of the conventional and hierarchical FeSAPO-11.
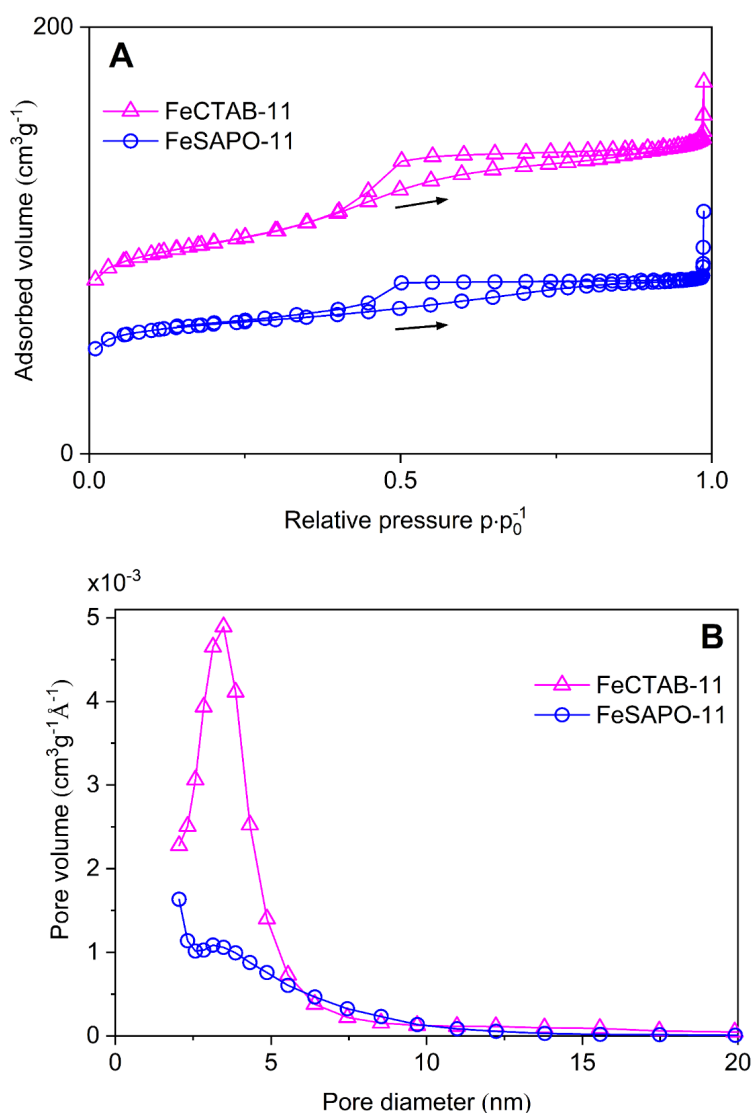

Fig. 3: Nitrogen physisorption isotherms (A) and BJH pore size distributions (B) for both FeSAPO-11s. For the pore size distributions, the adsorption branch of the BJH method was used.

A detailed account on the results from the XAS study has been provided in the electronic supplementary information (ESI, Section 2.0). Briefly, XANES (Fig. S2-1) indicated that iron was present as iron(III), while EXAFS refinements (Table S2-1) of the single shell that was found (Fig. S2-2), indicated that calcined FeSAPO-11 had 4 Fe-O neighbors at 1.95 Å whereas calcined FeCTAB-11 had 3 Fe-O neighbors at 1.93 Å. While these distances are slightly longer

compared to those of previously studied Fe(III)-incorporated zeolites (~1.85 Å),[32–34] they are similar to previously reported distances of iron- (1.91 Å)[35] and other transition metal-incorporated SAPOs (1.95 Å)[16] and do not correspond to Fe-O bonds in iron oxides. Furthermore and importantly, no Fe-Fe or Fe-O-Fe contributions could be found, indicating that isolated, single-site Fe(III) is present in calcined FeSAPO-11 and FeCTAB-11.

In summary, the FeSAPOs had an equally high crystallinity, were phase pure and had similar amounts of iron in the calcined samples. FeCTAB-11 had a significantly increased external surface area and mesopore volume compared to the corresponding surface area and pore volume of FeSAPO-11. In addition to a large feature in the BJH pore size distribution, the characterization results strongly indicated the presence and incorporation of mesopores into FeCTAB-11. Finally, XAS analysis indicated that both FeSAPOs had iron incorporated into their structures as iron(III). To the best of the authors' knowledge, this is the first reported successful synthesis of iron-incorporated hierarchical SAPO-11.

3.2 **Characterization of FeSAPOs by FTIR spectroscopy with CO adsorption**

Although there are several studies on the incorporation of iron into SAPO structures (mainly SAPO-34 and SAPO-37),[6,35–37] there are few detailed FTIR investigations on how the incorporated iron may interact with probe molecules such as carbon monoxide (CO). On the other hand, studies on iron-incorporated zeolites have shown that multiple interactions between iron and CO may occur depending on the valence state of the iron.[38–41] Specifically for Fe^{3+} for example, the interaction with CO is debated, with some authors suggesting that Fe^{3+} interacts readily with CO,[38,40,42] whereas others allege that Fe^{3+} cannot form bonds with CO.[41] The incorporation of iron into zeolites has also been reported to change band locations and generate new bands in the Brønsted region (3800 - 3200 cm^{-1}).[38,43] For instance, isomorphous substitution of Fe^{3+} into ZSM-5 shifted the location of the Brønsted band and resultantly decreased the acid strength of the zeolite,[38] whereas additional bands were discovered in the Brønsted region of iron(III)-incorporated H-BEA.[43] Lastly, previous reports have revealed that quaternary ammonium surfactant meso-SDAs may reduce[18] or increase[12] the acid site density of the resulting hierarchical SAPOs. In this study, X-ray absorption spectroscopy (XAS) investigations (ESI, Section 2.0) indicated that single site iron was present as Fe^{3+} in both FeSAPO-11 and FeCTAB-11. Thus, CO-FTIR investigations were employed to investigate the

presence of additional bands in the Brønsted region, possible Fe^{3+}-CO interactions, as well as if the acid site density and acid strength of the resulting FeSAPOs was affected by iron and mesopore incorporation. A detailed description of the interactions between CO and a reference SAPO-11 without metal (C-SAPO-11) can be found in the ESI, Section 1.4.

The results of the CO adsorption in the Brønsted region (3800 - 3200 cm^{-1}) are depicted in Fig. S1-5 as normalized difference spectra, where the clean vacuum spectra before CO adsorption have been subtracted from the spectra fully perturbed by similar amounts of CO. The typically reported bands for SAPO-11 were displayed by all samples: isolated silanol sites (Si-OH) at 3745 cm^{-1}, terminal P-OH groups at 3678 cm^{-1}, Brønsted acid sites (BAS) at approximately 3630 cm^{-1} and hydroxyl bands interacting with lattice oxygens at 3520 cm^{-1}.[44–46]

Table S1-3 gives an overview of the location of the observed bands in the Brønsted region for FeSAPO-11, FeCTAB-11 and a reference C-SAPO-11 without metal as well as the shifts, Δv_{OH}, between the high frequency BAS ($v_{Brönsted}$) and the BAS perturbed by CO ($v_{Brönsted*}$). The shifts of the samples were found to be between 260 and 266 cm^{-1}, where a BAS shift around 270 cm^{-1} is an average value for medium-strength SAPOs according to previous literature reports.[47,48] Thus, the acid strength of SAPO-11 was not significantly affected by the introduction of mesopores nor by the introduction of iron, matching previous reports on hierarchical SAPO-11[12,28] and iron-incorporated SAPOs,[6,36,37] respectively. Importantly, there were no additional bands observed in the Brønsted region of FeSAPO-11 and FeCTAB-11 that could be attributed to Fe^{3+}-OH. As previously mentioned for FeZSM-5, a previous study reported that bridging Si(OH)Fe groups were slightly red-shifted (3630 cm^{-1}) from the original BAS (3615 cm^{-1}),[40] however no such red-shifted band could be discerned for the FeSAPOs in this study. On the other hand, Fe^{3+}-OH bands have also previously been reported to occur between 3665 and 3674 cm^{-1} for other iron-incorporated zeolites.[38,39] This indicates that the bands may be present underneath the terminal P-OH group bands (3678 cm^{-1}) of FeSAPO-11 and FeCTAB-11.

The bands that appeared in the CO region (2200 - 2100 cm^{-1}) upon introduction of similar amounts of CO for FeSAPO-11, FeCTAB-11 and a reference C-SAPO-11 without metal are plotted in Fig. S1-6, with detailed values provided in Table S1-4. Both FeSAPOs had two main bands present at 2171 cm^{-1} and 2137 cm^{-1}, which according to previous reports on SAPOs are assigned to CO interacting with the Brønsted acid sites and liquid-like (physically adsorbed)

CO, respectively.[47,48] Furthermore, no additional bands that could be attributed to iron oxides (e.g. Fe_2O_3 at 2165 - 2170 cm^{-1})[40] could be discerned, further corroborating the XAS results on the successful incorporation of Fe^{3+} into the SAPO structure. However, including the previously mentioned bands, the FeSAPOs had an additional band at 2181 cm^{-1}. The exact designation of this band has been frequently debated, with some authors attributing it to carbonyls bonding with Fe^{2+},[39] whereas others claim that the band arises due to interactions between Fe^{3+} and CO.[40,42] An additional report[41] corroborates the former by alleging that Fe^{3+} cannot form carbonyl adducts via pi-backbonding due to the Fe^{3+}-ion's preference to form covalent bonds. The aforementioned report also mentioned that thermal pre-treatment in vacuum may cause reduction of Fe^{3+} to Fe^{2+}-ions, whereas another report[40] tentatively suggested that vacuum treated, partially reduced Fe^{3+} interacting with CO gives rise to bands at 2157 cm^{-1}. In this study however, no such band could be observed. Nevertheless, as XAS studies clearly showed that iron was incorporated as Fe^{3+} in the SAPO-11 structures, the band at 2181 cm^{-1} is ascribed to carbonyls interacting with Fe^{2+}-ions generated from autoreduction of Fe^{3+}-ions during the thermal vacuum pre-treatment of the FTIR experiments. Lastly, following the assumption of Fe^{2+} giving rise to the band at 2181 cm^{-1}, an estimate on the relative density of Fe^{2+}-sites in the samples was obtained by Gaussian peak fitting and subsequent integration of the peak corresponding to the 2181 cm^{-1} band (Fig. S1-7). It was found that FeSAPO-11 contained 1.8 times the density of Fe^{2+}-sites compared to FeCTAB-11, suggesting that the iron present in FeCTAB-11 may be more resistant to thermal vacuum autoreduction compared to FeSAPO-11.

A relative estimate on the acid density in each sample was obtained according to previously reported methods[18] and has been given in Table 2, whereas detailed values (as well as a comparison to a reference C-SAPO-11 without metal) have been provided in Table S1-5. Evidently, FeCTAB-11 had slightly increased densities of weak acid sites (WAS, isolated silanols, 1.2) and P-OH groups (1.1) compared to FeSAPO-11 (WAS and P-OH, 1.0). On the other hand, the hierarchical FeCTAB-11 had a significantly reduced density of BAS (0.31) compared to the conventional FeSAPO-11 (1.0). As a note on the WAS density, the increased density of WAS for the hierarchical FeCTAB-11 may indicate the presence of such sites in mesopores.[9,18] The density of P-OH groups was also slightly larger for the hierarchical FeCTAB-11 compared to the conventional FeSAPO-11, where an increase in P-OH group density may be expected for smaller SAPO particles.[45,49] Indeed, the particle size of FeCTAB-11 was much smaller (9 ± 3 μm) compared to FeSAPO-11 (21 ± 10 μm) and the slight increase

in P-OH group density is therefore assigned to differences in particle size. Finally, regarding the Brønsted acid sites, the introduction of mesopores via a quaternary ammonium surfactant has previously been shown to reduce the density of acid sites for SAPOs,[18] which is in accordance with the results obtained for FeCTAB-11 in this study.

Table 2: Summary of SEM and FTIR characterization results for the FeSAPO-11s.

Sample	Particle size (µm)	BAS shift (cm^{-1})	ρ^a (BAS) (a.u.)	ρ (WAS) (a.u.)	ρ (P-OH)^b (a.u.)
FeSAPO-11	21 ± 10	266	1	1	1
FeCTAB-11	9 ± 3	260	0.31	1.2	1.1

[a]Relative density of acid sites.

[b]P-OH groups.

In summary, the incorporation of iron and mesopores did not have a significant effect on the acid strength of the SAPO-11 system. However, the acid density of the hierarchical FeCTAB-11 was significantly reduced compared to that of FeSAPO-11 due to the introduction of mesopores. Furthermore, while the presence of Fe^{3+}-OH bands could not be discerned, the bands were inferred to be present underneath the terminal P-OH bands of FeSAPO-11 and FeCTAB-11. Notably, some Fe^{3+} may have been reduced to Fe^{2+} during the vacuum pre-treatment of the FTIR experiments, resulting in Fe^{2+}-CO interactions for both FeSAPO-11 and FeCTAB-11. Lastly and importantly, no additional bands that could be attributed to iron oxides were detected.

3.3 Characterization of FeSAPOs by CO₂-TPD

The incorporation of metals in zeolite and zeotype frameworks may create basic sites where the metal cation becomes a Lewis acid and lattice oxygen becomes a Lewis base.[8] While this is more prevalent for alkali and earth alkali metals,[8,50] it may also occur for isomorphous substitution with trivalent transition metal cations such as Fe^{3+}.[51] Thus, to investigate if the iron-incorporated SAPO-11s had basic sites, carbon dioxide temperature-programmed desorption (CO₂-TPD) was conducted.

The detailed results of the CO_2-TPD investigations are reported in Table 3 while Fig. 4 shows the intensity of desorbed CO_2 over the measured temperature range (120 °C to 840 °C). A comparison with a conventional SAPO-11 reference (without metal) has also been provided in the ESI (Table S1-6).

Table 3: Summary of CO_2-TPD analyses on FeSAPO-11 and FeCTAB-11. The relative peak areas are normalized with respect to the peak area of FeSAPO-11.

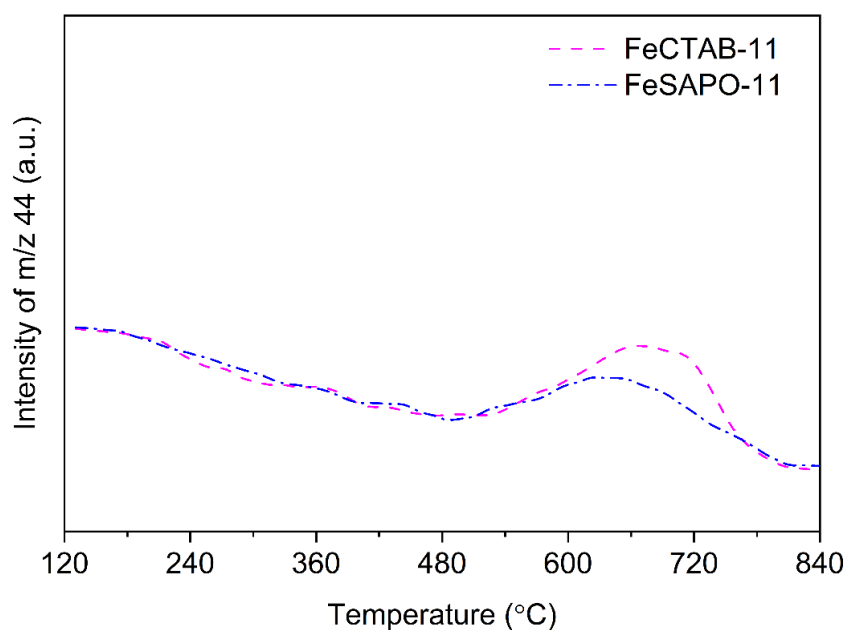| Sample	Peak center (temperature, °C)	Relative peak area (a.u.)	Peak height (a.u.)
FeSAPO-11	653	1	0.22
FeCTAB-11	679	1.5	0.36

Fig. 4: CO_2-TPD curves for FeCTAB-11 and FeSAPO-11 showing the amount of desorbed CO_2 as a function of temperature.

A significant peak at elevated temperatures (600 - 700 °C) indicated the presence of strong basic sites for both FeSAPO-11 and FeCTAB-11. Furthermore, the relative areas under the peaks (Table 3) showed that FeCTAB-11 had 1.5 times the number of basic sites compared to FeSAPO-11. Based on the assumption that basic sites are exclusively introduced by

incorporation of Fe^{3+} (in accordance to Kosinov et al.[51]), this may indicate that some of the iron in FeSAPO-11 has autoreduced to Fe^{2+} as a result of the thermal pre-treatment in argon. This has been previously reported for other iron exchanged zeolites[52] and also corroborates the results from the FTIR investigations. It should be noted that FeCTAB-11 seemingly had slightly stronger basic sites (679 °C) compared to FeSAPO-11 (653 °C). However, when considering the range of medium-strength (200 °C - 400 °C) and weak (~100 °C) basic sites,[7,53,54] the strength of the basic sites for FeSAPO-11 and FeCTAB-11 were deemed to be equivalent. Lastly, it should be mentioned that the strength of the basic sites of the FeSAPOs in this study was in the upper range of previous reports on basic sites in metal-incorporated zeolites and SAPOs.[7,53,54] In summary, the incorporation of Fe^{3+} into conventional and hierarchical SAPO-11 caused strong basic sites to be generated in the SAPO framework. To the best of the authors' knowledge, this has not previously been reported for transition metals incorporated into SAPOs. As basicity is a local property,[55] these basic sites are also most likely situated closely to the iron species and may therefore be used to locate the topological position of the incorporated iron.

3.4 **Model reactions over FeSAPO-11**

A catalytic model reaction which has shown promise for evaluating the pore topology and WAS location of hierarchical SAPOs, is the vapor phase isomerization of cyclohexanone oxime (Beckmann rearrangement, BMR).[9] Previous studies have indicated that the product distribution of the BMR is sensitive to metal incorporation and the presence of basic sites,[56–58] which may benefit the investigation of the location of the metal species. As such, in this study the location of the metal species in the FeSAPOs was probed by utilizing the BMR model reaction. As the FeSAPOs contained comparable amounts of iron (~2.0 wt.%), direct comparison of the two molecular sieves was deemed to be justifiable.

3.4.1 Vapor phase isomerization of cyclohexanone oxime model reaction

From CO_2-TPD, it was established that the incorporation of iron generated strong basic sites in the SAPO-11 framework, where the topological location of the iron sites may be found by probing the location of the basic sites due to basicity being a local property.[55]. As previously mentioned, the BMR is a model reaction that is sensitive to the presence of basic sites. Indeed,

compared to a purely acidic catalyst, the presence of strong basic sites on a catalyst is known to cause a significant shift in the product distribution of the BMR due to the emergence of side reactions.[57,58] These side reactions produce products that may condense and polymerize with each other over basic sites, causing pore blockage and deactivation due to a significantly increased formation of coke.[57,58] This may result in two scenarios depending on where the basic sites are located: firstly, if the basic sites are situated in the micropores of the catalysts, the amount of generated coke will be limited by the microporous system. More importantly, the side reactions cannot proceed once the micropores are blocked as the basic sites will no longer be accessible to the reactants. Lastly, if the basic sites are situated in highly accessible mesopores, the side reactions should be able to proceed more freely, leading to a high generation of coke as well as a higher percentage of by-products being formed for longer periods of time. Thus, in this study, the BMR was applied to investigate the location of the iron species in FeSAPO-11 and FeCTAB-11 by utilizing the product selectivity of the model reaction to probe the location of the basic sites.

A detailed account on the conversion and lifetime of FeSAPO-11 and FeCTAB-11 in the BMR model reaction has been provided in the ESI (Section 3.0). Briefly, Fig. S3-1 shows that both catalysts had high initial conversions (>60%) but deactivated over time due to large deposits of carbonaceous species.

The initial and 7-hour selectivities from the BMR for FeSAPO-11 and FeCTAB-11 are plotted in Fig. 5, whereas detailed values have been provided in Table S3-1. The main product for both FeSAPOs regardless of time on stream was cyclohexanone, which matches previous studies on iron-containing SAPO-11 catalysts[56] but is in stark contrast to results for conventional SAPO-11, which mostly produces ε-caprolactam.[59] More importantly however, by-products (excluding cyclohexanone) were a large part of the initial product distribution for both FeCTAB-11 (33%) and FeSAPO-11 (23%). Notably, the main by-product for both iron-incorporated catalysts was aniline, where FeCTAB-11 produced a larger initial quantity (20%) compared to FeSAPO-11 (12%).
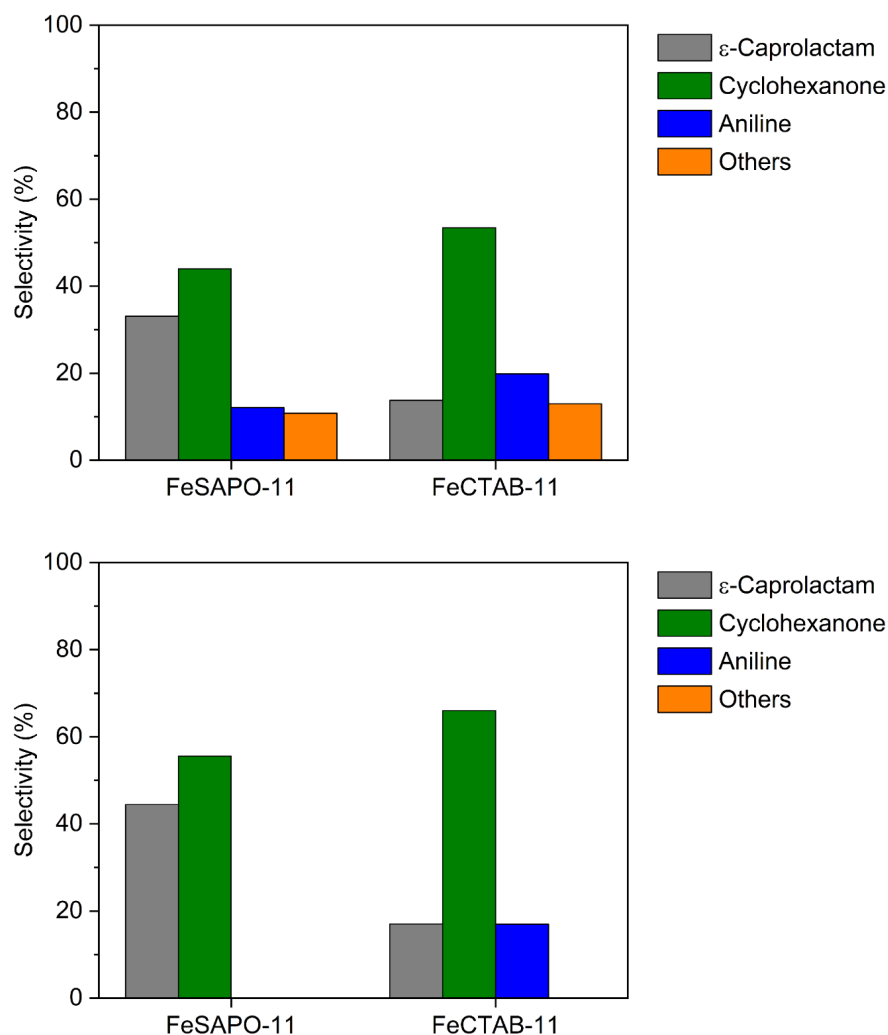
Fig. 5: Initial (top) and 7-hour (bottom) product distributions for the BMR model reaction. Detailed values have been given in Table S3-1 in the ESI.

In order to evaluate the location of the iron species, the lifetime of products that are generated by basic sites should be monitored and according to previous reports,[57,58] the production of both cyclohexanone and aniline is most prevalent over catalysts with basic sites. However, other reports have indicated that cyclohexanone may also be formed by interacting with WAS such as isolated silanols (SiOH).[60] Indeed, previous studies on SAPO-11 have noted the presence of cyclohexanone in the product distribution of the SAPO.[59] On the other hand, the same study, as well as others,[9] have not reported aniline as a by-product of the BMR over SAPOs. It should also be noted that this is not an effect of shape selectivity as aniline (~0.58 nm)[61] is roughly the same size as the reactant, cyclohexanone oxime (~0.58 nm)[62]. Thus, as aniline has not been presented as a by-product in previous reports on the BMR over non-metal-

containing SAPOs, it was chosen to represent the activity of the basic sites of FeSAPO-11 and FeCTAB-11 in this study.

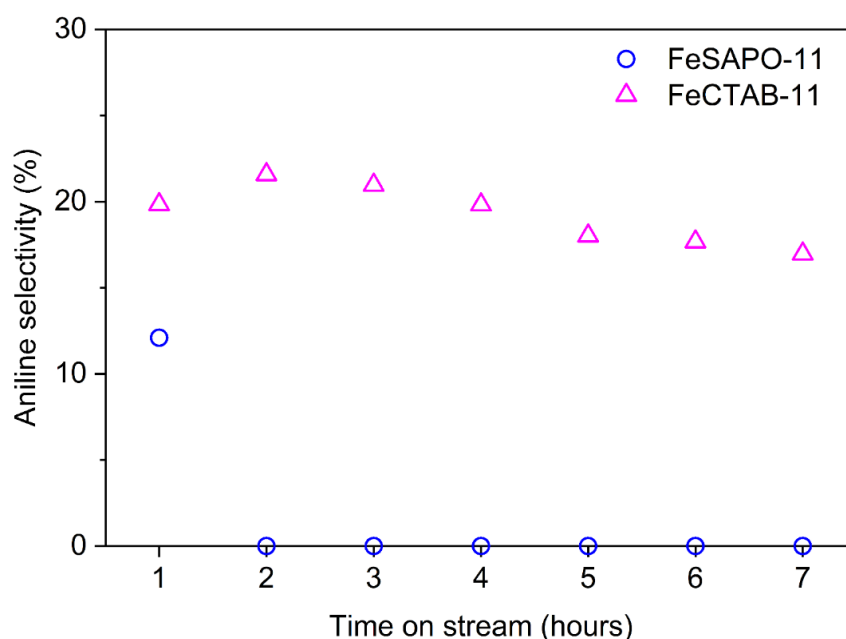The selectivity of aniline throughout the BMR has been given in Fig. 6.

Fig. 6: Aniline selectivity as a function of time on stream for FeSAPO-11 and FeCTAB-11 during the BMR model reaction.

Clearly, the selectivity was different for the two catalysts, with FeSAPO-11 only producing aniline for 1 hour on stream whereas FeCTAB-11 produced stable amounts of aniline throughout the model reaction (7 hours). In order to elucidate if the differences in the lifetime of aniline production for the iron-incorporated catalysts was related to the location of the basic sites, key differences in characteristic properties that are related to the formation of aniline should be investigated. According to a previous study on the vapor phase BMR,[58] the production of aniline from cyclohexanone oxime requires the presence of both an intermediate-strength acid site and a basic site, where the former corresponds to the strength of the BAS of SAPO-11. Thus, as previous studies on zeolites and SAPOs have noted that the selectivity of the BMR is independent of particle size,[9,59,63] the acidity and basicity of the iron-incorporated SAPOs were evaluated with respect to the lifetime of aniline production.

In this study, FeSAPO-11 had a higher BAS density (1.0) than FeCTAB-11 (0.31) where the latter also had the longest lifetime for aniline production, possibly hinting at an inverse relationship between the two parameters. However, the main function of the BAS for aniline production is to initially activate cyclohexanone oxime.[58] In other words, whereas an increased acid density may result in a higher initial production of aniline, the acid density should be independent of the lifetime of aniline production. Indeed, a previous report on ZSM-5 and zeolite Beta indicated that while the former produced larger amounts of aniline for increased acid densities, there was no trend to be found between the lifetime of aniline production and acid densities of the latter.[64] Thus in accordance to previous reports, the lifetime of aniline production was considered to be independent of the acid density of FeSAPO-11 and FeCTAB-11. Lastly, as the acid strength of the iron-incorporated SAPOs was similar, the lifetime of aniline production was altogether deemed to be independent of the acidic properties of FeSAPO-11 and FeCTAB-11.

Regarding the basicity of the iron-incorporated samples, the CO_2-TPD results (Table 3) indicated that the hierarchical FeCTAB-11 contained slightly more basic sites (1.5) than FeSAPO-11 (1.0). This is reflected in the correspondingly larger initial selectivity towards aniline for the hierarchical FeCTAB-11 (20%) compared to FeSAPO-11 (12%). However, the difference in basic site density cannot explain why the selectivity of aniline suddenly dropped for FeSAPO-11. This is also true for the strength of the basic sites, which was similar for the two samples. In other words, the increased lifetime of aniline production for FeCTAB-11 cannot be explained by differences in the acidic or basic properties of the samples. Finally, as post-catalysis XRD (Fig. S3-2) confirmed that neither catalyst collapsed during the model reaction, the lifetime of aniline production must be related to the location of the active sites and implicitly, the location of the iron species.

Whereas the production of aniline rapidly stopped for FeSAPO-11, FeCTAB-11 continuously produced a stable amount of aniline, indicating that the basic sites of the hierarchical sample were more accessible than for FeSAPO-11. This was confirmed by post-catalysis analyses, where post-catalysis nitrogen physisorption (Fig. S3-3) revealed that the micropores of both catalysts were completely congested after the reaction, suggesting that the active sites situated in these pores were mostly inaccessible. Clearly, Fig. 6 illustrates that FeCTAB-11 still produced stable amounts of aniline even though its micropores were blocked, demonstrating that FeCTAB-11 indeed had highly accessible basic sites most likely situated in the mesopores

of the sample. Finally, TGA-MS on spent samples (Table S3-2 and Fig. S3-4) showed that FeCTAB-11 had amassed almost twice the amount of coke (7.5%) of FeSAPO-11 (4.9%). While this may be explained by the increased density of basic sites for FeCTAB-11 (1.5) compared to FeSAPO-11 (1.0), it may also indicate that FeCTAB-11 allowed for an overall increased polymerization of the products from the reaction. As polymerization reactions for the BMR typically happen over basic sites (*vide supra*),[57,58] the increased amount of coke for FeCTAB-11 may serve as an additional, albeit vague indicator for the presence of highly accessible basic sites for FeCTAB-11. In summary, whereas FeSAPO-11 exclusively had iron species situated in its micropores, FeCTAB-11 also had iron species most likely situated in highly accessible mesopores.

As a note on pore topology, as previously mentioned the formation of aniline initially requires activation of cyclohexanone oxime by an acid site.[58] Thus, by investigating the location of the acid sites, a potential indication on the pore topology can be obtained. This was done by utilizing the methanol-to-hydrocarbons (MTH) model reaction.

3.4.2 Methanol-to-hydrocarbons model reaction

The MTH model reaction was first and foremost conducted to investigate the location of the Brønsted acid sites for FeSAPO-11 and FeCTAB-11. According to previously reported methods,[18] the location of the BAS may be probed by evaluating the selectivity of the MTH model reaction. Here, an increased production of products that are larger than the micropores of the SAPO-11 structure (AEL, 0.40 nm × 0.65 nm)[17] may be expected if BAS are located in mesopores. Thus, in this study, mainly the selectivity of the iron-incorporated SAPOs for the MTH model reaction was considered. A brief account on the activity and lifetime, as well as the location of the WAS, may be found in the ESI (Section 4.0).

The initial and 20-hour selectivity of FeSAPO-11 and FeCTAB-11 have been plotted in Fig. 7, whereas detailed values have been provided in Table S4-1. The main product for both samples regardless of time on stream was dimethyl ether (DME), which is contrary to previous studies on metal-containing SAPO-34 and SAPO-11,[36,65] where addition of metal shifted the selectivity towards olefins. More importantly, FeCTAB-11 did not produce any products that were larger than the micropores of the AEL structure, indicating that the hierarchical FeCTAB-

11 most likely did not have BAS in its mesopores. This also matches a previous study on the location of acid sites for hierarchical SAPO-11 hydrothermally synthesized with CTAB as a meso-SDA.[19]
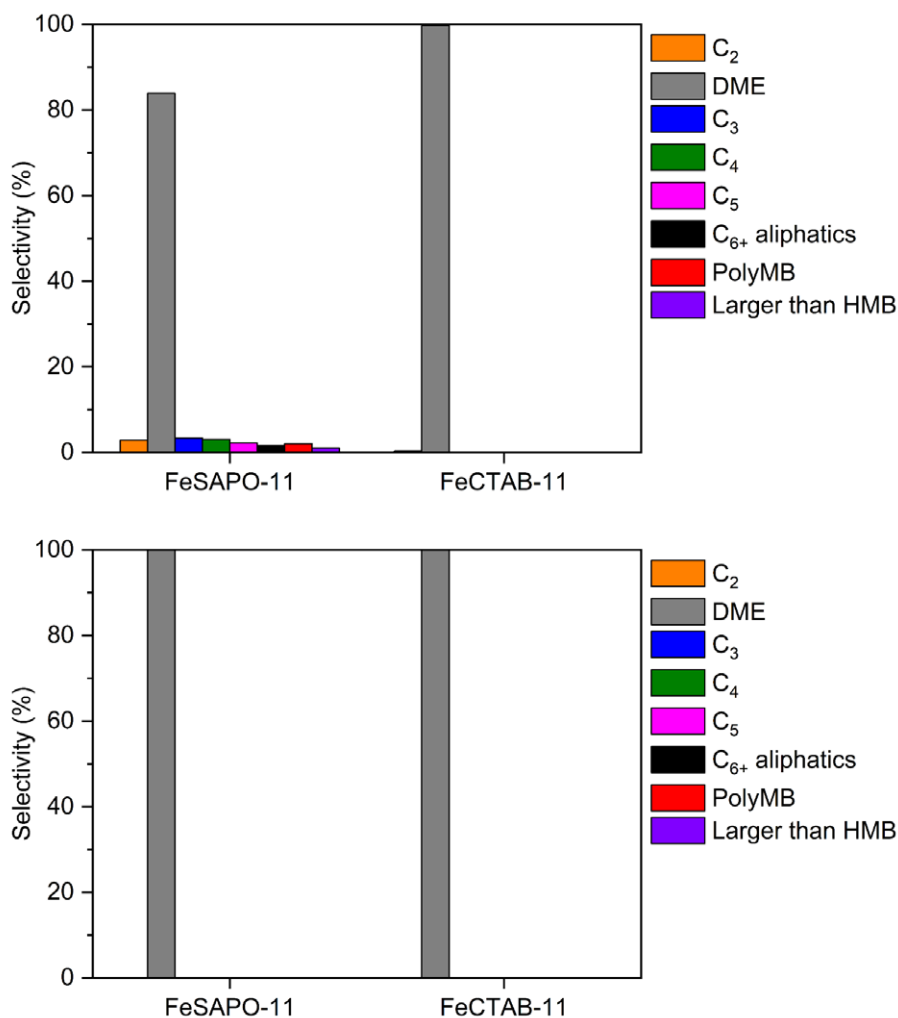

Fig. 7: Initial (top) and 20-hour (bottom) product distributions for the MTH model reaction. Detailed values have been given in Table S4-1 in the ESI.

Regarding the pore topology and as previously stated, the BMR model reaction depends on both acid sites and basic sites to produce base-catalyzed products such as aniline.[58] Thus, as the BMR and MTH model reactions have respectively established that FeCTAB-11 has basic sites in mesopores and BAS in micropores, the micropores and mesopores of FeCTAB-11 must be interconnected for the production of aniline to occur.

4. Conclusions

23

The first successful synthesis procedure for iron-incorporated hierarchical SAPO-11 has been developed using a hydrothermal approach with CTAB as a meso-SDA. The bimodal porosity and incorporation of Fe^{3+} in the hierarchical FeCTAB-11 was verified during a comprehensive characterization process where results were compared to the conventional reference FeSAPO-11. Remarkably, CO_2-TPD indicated that functionalization of the SAPO-11 framework with iron(III) resulted in the first reported formation of basic sites in SAPOs with isomorphously substituted transition metals. These basic sites were utilized in the vapor phase isomerization of cyclohexanone oxime (Beckmann rearrangement, BMR) to probe the topological location of Fe^{3+} incorporated in the hierarchical SAPO-11 framework. The base-catalyzed BMR revealed that FeSAPO-11 had basic sites, and hence Fe^{3+}-sites, located in the micropores whereas FeCTAB-11 had highly accessible Fe^{3+}-sites most likely located in the mesopores of its structure. Lastly, the pore connectivity was elucidated by utilizing the base-catalyzed BMR's dependency on both Brønsted acid sites (BAS) and basic sites, where the BAS were revealed by the methanol-to-hydrocarbons (MTH) model reaction to be mainly situated in the micropores for both FeSAPO-11 and FeCTAB-11. As the basic sites of FeCTAB-11 most likely were located in mesopores, this indicated that the micropores and mesopores of FeCTAB-11 must have been connected for production of base-catalyzed products to occur. Clearly, the MTH and BMR model reactions are powerful characterization tools that are highly capable of probing multiple characteristics of the hierarchical SAPO-11 system. While SAPO-11 is an ideal, one-dimensional model system, it's feasible that these ad hoc model reactions for locating metal species and probing pore connectivity can be expanded to other, more complicated metal-incorporated systems.

Author contributions

Daniel Ali: Conceptualization, Methodology, Writing – Original Draft. **Zhihui Li:** Resources. **Muhammad Mohsin Azim:** Writing – Review & Editing. **Hilde Lea Lein:** Writing – Review & Editing. **Karina Mathisen:** Conceptualization, Writing – Review & Editing, Supervision, Funding acquisition.

Conflicts of interest

There are no conflicts to declare.

Acknowledgements

Notes and references

1. M. Cortés-Reyes, E. Finocchio, C. Herrera, M. A. Larrubia, L. J. Alemany and G. Busca, *Microporous Mesoporous Mater.*, 2017, **241**, 258-265.

2. N. Azuma, C. W. Lee and L. Kevan, *Am. J. Phys. Chem.*, 1994, **98**, 1217-1221.

3. K. Mathisen, D. G. Nicholson and M. Stockenhuber, *Microporous Mesoporous Mater.*, 2005, **84**, 261-274.

4. R. Martínez-Franco, M. Moliner and A. Corma, *J. Catal.*, 2014, **319**, 36-43.

5. D. R. Dubois, D. L. Obrzut, J. Liu, J. Thundimadathil, P. M. Adekkanattu, J. A. Guin, A. Punnoose and M. S. Seehra, *Fuel Process. Technol.*, 2003, **83**, 203-218.

6. M. Sedighi, M. Ghasemi, M. Sadeqzadeh and M. Hadi, *Powder Technol.*, 2016, **291**, 131-139.

7. M. Sedighi, M. Ghasemi and A. Jahangiri, *Korean J. Chem. Eng.*, 2017, **34**, 997-1003.

8. S. Ordóñez and E. Diaz, in *Handbook of Zeolites*, ed. T. W. Wong, Nova Science Publishers, Inc., 2009, ch. 3, pp. 51-66.

9. S. H. Newland, W. Sinkler, T. Mezza, S. R. Bare, M. Carravetta, I. M. Haies, A. Levy, S. Keenan and R. Raja, *ACS Catal.*, 2015, **5**, 6587-6593.

10. W. Zhao, H. Yang, Z. Li, L. Zhang, X. Lin, H. Fu, Z. Liu and C. Wang, *Mater. Res. Express*, 2020, **7**, 085009.

11. S. Tao, X. Li, G. Lv, C. Wang, R. Xu, H. Ma and Z. Tian, *Catal. Sci. Technol.*, 2017, **7**, 5775-5784.

12. P. Zhang, H. Liu, Y. Yue, H. Zhu and X. Bao, *Fuel Process. Technol.*, 2018, **179**, 72-85.

13. M. D. Rami, M. Taghizadeh and H. Akhoundzadeh, *Microporous Mesoporous Mater.*, 2019, **285**, 259-270.

14. A. Z. Varzaneh, J. Towfighi and S. Sahebdelfar, *Microporous Mesoporous Mater.*, 2016, **236**, 1-12.

15. A. Zeinali Varzaneh, J. Towfighi and M. Saei Moghaddam, *React. Kinet., Mech. Catal.*, 2019, **128**, 1043-1063.

16. G. Sørli, M. M. Azim, M. Ronning and K. Mathisen, *Phys. Chem. Chem. Phys.*, 2021, **23**, 16785-16794.

17. R. W. Grosse-Kunstleve, S. S. Prokic, M. M. J. Treacy, J. B. Higgins and C. Baerlocher, Database of Zeolite Structures, http://www.iza-structure.org/databases/, (accessed June 2022).

18. D. Ali, C. R. Zeiger, M. M. Azim, H. L. Lein and K. Mathisen, *Microporous Mesoporous Mater.*, 2020, **306**, 110364.

19. D. Ali, Z. Li, M. M. Azim, H. L. Lein and K. Mathisen, *Microporous Mesoporous Mater.*, 2022, **329**, 111550.

20. S. Zhang, S.-L. Chen, P. Dong, G. Yuan and K. Xu, *Appl. Catal., A*, 2007, **332**, 46-55.

21. B. Ravel and M. Newville, *J. Synchrotron Radiat.*, 2005, **12**, 537-541.

22. S. Tomic, B. G. Searle, A. Wander, N. M. Harrison, A. J. Dent, J. F. W. Mosselmans, J. E. Inglesfield, *New Tools for the Analysis of EXAFS: The DL EXCURV Package. CCLRC Technical Report*, 2005.

23. S. Andonova, S. Tamm, C. Montreuil, C. Lambert and L. Olsson, *Appl. Catal., B*, 2016, **180**, 775-787.

24. J. W. Niemantsverdriet, *Spectroscopy in Catalysis: An Introduction*, Wiley-VCH Verlag GmbH & Co. KGaA, Weinheim, 2007.

25. L. Han, Y. Liu, F. Subhan, X. Liu and Z. Yan, *Microporous Mesoporous Mater.*, 2014, **194**, 90-96.

26. P. Liu, J. Ren and Y. Sun, *Microporous Mesoporous Mater.*, 2008, **114**, 365-372.

27. S. Said and M. T. Zaky, *Catal. Lett.*, 2019, **149**, 2119-2131.

28. L. Yang, H. Li, J. y. Fu, M. Li, C. Miao, Z. Wang, P. Lv and Z. Yuan, *RSC Adv.*, 2019, **9**, 34457-34464.

29.   L. Guo, X. Bao, Y. Fan, G. Shi, H. Liu and D. Bai, *J. Catal.*, 2012, **294**, 161-170.

30.   M. Thommes, K. Kaneko, V. Neimark Alexander, P. Olivier James, F. Rodriguez-Reinoso, J. Rouquerol and S. W. Sing Kenneth, *Pure Appl. Chem.*, 2015, **87**, 1051.

31.   M. Thommes, *Chem. Ing. Tech.*, 2010, **82**, 1059-1073.

32.   B. Ma, A. Fernandez-Martinez, A. Mancini and B. Lothenbach, *Cem. Concr. Res.*, 2021, **140**, 106304.

33.   K. Yong Sig and A. Wha Seung, *Microporous Mater.*, 1997, **9**, 131-140.

34.   Y. S. Ko, H. T. Jang and W. S. Ahn, *Korean J. Chem. Eng.*, 2008, **25**, 1286-1291.

35.   A. Turrina, A. Iulian Dugulan, J. E. Collier, R. I. Walton, J. L. Casci and P. A. Wright, *Catal. Sci. Technol.*, 2017, **7**, 4366-4374.

36.   K. Mirza, M. Ghadiri, M. Haghighi and A. Afghan, *Microporous Mesoporous Mater.*, 2018, **260**, 155-165.

37.   K. V. V. S. B. S. R. Murthy, S. J. Kulkarni, M. Chandrakala, K. V. V. Krishna Mohan, P. Pal and T. S. R. Prasada Rao, *J. Porous Mater.*, 2010, **17**, 185-196.

38.   K. Hadjiivanov, in *Advances in Catalysis*, ed. F. C. Jentoft, Academic Press, vol. 57, 2014, ch. 2, pp. 99-318.

39.   E. Ivanova, M. Mihaylov, K. Hadjiivanov, V. Blasin-Aubé, O. Marie, A. Plesniar and M. Daturi, *Appl. Catal., B*, 2010, **93**, 325-338.

40.   A. Zecchina, F. Geobaldo, C. Lamberti, S. Bordiga, G. Turnes Palomino and C. Otero Areán, *Catal. Lett.*, 1996, **42**, 25-33.

41.   K. I. Hadjiivanov and G. N. Vayssilov, in *Advances in Catalysis*, Academic Press, vol. 47, 2002, ch. 4, pp. 307-511.

42.   M. Ma, H. Noei, B. Mienert, J. Niesel, E. Bill, M. Muhler, R. A. Fischer, Y. Wang, U. Schatzschneider and N. Metzler-Nolte, *Chem. - Eur. J.*, 2013, **19**, 6785-6790.

43.   R. Kefirov, E. Ivanova, K. Hadjiivanov, S. Dzwigaj and M. Che, *Catal. Lett.*, 2008, **125**, 209.

44.   P. Mériaudeau, V. A. Tuan, V. T. Nghiem, S. Y. Lai, L. N. Hung and C. Naccache, *J. Catal.*, 1997, **169**, 55-66.

45.   P. Mériaudeau, V. A. Tuan, F. Lefebvre, V. T. Nghiem and C. Naccache, *Microporous Mesoporous Mater.*, 1998, **22**, 435-449.

46.   K.-H. Schnabel, R. Fricke, I. Girnus, E. Jahn, E. Löffler, B. Parlitz and C. Peuker, *J. Chem. Soc., Faraday Trans.*, 1991, **87**, 3569-3574.

47.   F. Bleken, M. Bjørgen, L. Palumbo, S. Bordiga, S. Svelle, K.-P. Lillerud and U. Olsbye, *Top. Catal.*, 2009, **52**, 218-228.

48.   M. Westgård Erichsen, S. Svelle and U. Olsbye, *J. Catal.*, 2013, **298**, 94-101.

49.   M. G. Abraha, X. Wu and R. G. Anthony, in *Stud. Surf. Sci. Catal.*, eds. G. F. Froment and K. C. Waugh, Elsevier, Amsterdam, vol. 133, 1 edn., 2001, pp. 211-218.

50.   H. Sato, N. Ishii, K. Hirose and S. Nakamura, in *Stud. Surf. Sci. Catal.*, eds. Y. Murakami, A. Iijima and J. W. Ward, Elsevier, Amsterdam, vol. 28, 1986, pp. 755-762.

51.   N. Kosinov, C. Liu, E. J. M. Hensen and E. A. Pidko, *Chem. Mater.*, 2018, **30**, 3177-3198.

52.   F. Gao, *Catalysts*, 2020, **10**, 1324.

53.   X. Guan, F. Zhang, G. Wu and N. Guan, *Mater. Lett.*, 2006, **60**, 3141-3144.

54.   J. Chen, X. Wang, D. Wu, J. Zhang, Q. Ma, X. Gao, X. Lai, H. Xia, S. Fan and T.-S. Zhao, *Fuel*, 2019, **239**, 44-52.

55.   D. B. Akolekar, M. Huang and S. Kaliaguine, *Zeolites*, 1994, **14**, 519-522.

56.   K. V. V. S. B. S. R. C. Murthy, M.; Kulkarni, S.J.; Raghavan, K.V., *Indian J. Chem. Technol.*, 2001, **8**, 368-370.

57.   T. Curtin, J. B. McMonagle, M. Ruwet and B. K. Hodnett, *J. Catal.*, 1993, **142**, 172-181.

58.   T. Curtin and B. K. Hodnett, in *Stud. Surf. Sci. Catal.*, eds. M. Guisnet, J. Barbier, J. Barrault, C. Bouchoule, D. Duprez, G. Pérot and C. Montassier, Elsevier, Amsterdam, vol. 78, 1993, pp. 535-542.

59.   P. S. Singh, R. Bandyopadhyay, S. G. Hegde and B. S. Rao, *Appl. Catal., A*, 1996, **136**, 249-263.

60.   K. Chaudhari, R. Bal, A. J. Chandwadkar and S. Sivasanker, *J. Mol. Catal. A: Chem.*, 2002, **177**, 247-253.

61.   E. Titus, A. K. Kalkar and V. G. Gaikar, *Sep. Sci. Technol. (Philadelphia, PA, U. S.)*, 2002, **37**, 105-125.

62.   Y. Chu, P. Ji, X. Yi, S. Li, P. Wu, A. Zheng and F. Deng, *Catal. Sci. Technol.*, 2015, **5**, 3675-3681.

63.   J. S. Reddy, R. Ravishankar, S. Sivasanker and P. Ratnasamy, *Catal. Lett.*, 1993, **17**, 139-144.

64.   K.-H. Ouyang, C.-W. Chen and A.-N. Ko, *J. Chin. Chem. Soc. (Weinheim, Ger.)*, 2001, **48**, 137-144.

65.   Z. Zhu, M. Hartmann and L. Kevan, *Chem. Mater.*, 2000, **12**, 2781-2787.